Second-order Raman scattering in germanium in the vicinity of the E_1, $E_1 + \Delta_1$ edges

M. A. Renucci, J. B. Renucci,* R. Zeyher, and M. Cardona
Max-Planck-Institut für Festkörperforschung, Stuttgart, Federal Republic of Germany
(Received 28 May 1974)

The resonance of the Γ_1 and $\Gamma_{25'}$ components of the second-order Raman spectrum of germanium has been measured in the vicinity of the E_1, $E_1 + \Delta_1$ edges. Particular emphasis was paid to the features corresponding to creation of 2TA(X) phonons, 2TO(L) phonons, and the anomalous peak due to 2TO(Γ) phonons. This anomalous peak disappears below the resonant gap and is attributed to an iterative process involving the first-order electron-phonon interaction taken to second order. The remaining resonant features are due to the second-order interactions taken to first order and thus are structurally analogous to the first-order processes. However, because of different contributions of two-band (intervalley) and three-band (intravalley) processes, radically different line shapes can result for these resonances. From these measurements, several electron–two-phonon coupling constants are determined.

INTRODUCTION

Within the past few years, resonance Raman scattering in the neighborhood of the E_0 and E_1 edges of tetrahedral semiconductors has received considerable attention.[1–3] The materials and the edges under study were chosen so as to occur in a region where a tight mesh of laser lines is available (Ar^+, Kr^+, He-Ne, He-Cd) or where continuously tunable cw[4,5] or pulsed[6] lasers are known to operate. For germanium, the prototype of the tetrahedral family, the E_0 gap occurs in a region (0.8 eV) not accessible to tunable lasers. While this gap has not been studied in resonant Raman scattering, the behavior of the resonances (both first and second order) can be inferred from the results obtained for GaP.[7]

The band structure of germanium is shown in Fig. 1. The $E_0 - E_0 + \Delta_0$ gap occurs between the $\Gamma_{25'}$ top of the valence band, split by spin-orbit interaction into Γ_8^+ and Γ_7^+, and the $\Gamma_{2'}$ conduction band. According to our experience with GaP we expect for the resonance of the first-order Raman phonon ($\Gamma_{25'}$) a sharp peak near E_0, due to the splitting of the Γ_8^+ degeneracy by the phonon distortion, and a weaker resonance near $E_0 + \Delta_0$ due to the coupling of Γ_8^+ with Γ_7^+ by the phonons. Neglecting the Raman frequency shift with respect to the relevant electronic energies, the leading singular term in the E_0 resonance has the form $|\omega - \omega_0|^{-1}$ and that in the $E_0 + \Delta_0$ resonance has the form $|\omega - \omega_0|^{1/2}$. Both these resonances depend on only one electron-phonon coupling constant (also called deformation potential) usually designated as d_0.[8] The three independent components of the second-order Raman spectrum, (Γ_1, $\Gamma_{25'}$, Γ_{12}) are expected to resonate in different ways. The $\Gamma_{25'}$ and Γ_{12} components should resonate with the same shape as the first-order phonon; the resonant strength, however, is given by different parameters designated as $D_{25'}$ and D_{12}. The Γ_1 component has strong $|\omega - \omega_0|^{-1}$-like resonances both at E_0 and $E_0 + \Delta_0$ since both gaps are modulated by symmetry-preserving perturbations (i.e., Γ_1). The strength of these resonances is determined by the deformation potential D_1.[7] It was shown in Ref. 7 that the deformation potentials D_1 and $D_{25'}$ are very large and, correspondingly, that the integrated strength of the second-order scattering is only an order of magnitude below that of the first-order line.

While the $E_0 - E_0 + \Delta_0$ gap of germanium is, at present, inaccessible to resonant Raman work, the $E_1 - E_1 + \Delta_1$ gap occurs in a rather convenient region (2.1–2.3 eV at 300 K), in which many gas laser lines and cw tunable dye lasers are available.[9] As shown in Fig. 1, this gap corresponds to transitions along most of the $\langle 111 \rangle$ directions of the Brillouin zone between the nearly parallel Λ_3 valence bands (split by spin-orbit interaction) and the Λ_1 conduction bands. The properties and algebra of these transitions are discussed in Ref. 8. The shape and strength of E_1, $E_1 + \Delta_1$ resonance of the first-order Raman phonon are determined by two processes, "interband" and "intraband," characterized by two independent deformation potentials. The "interband" process corresponds to the splitting of the [111] E_1, $E_1 + \Delta_1$ gaps from the equivalent gaps along $[\bar{1}11]$, $[1\bar{1}1]$, $[11\bar{1}]$, produced by a phonon polarized along [111]. This process is determined by a deformation potential called $d^5_{1,0}$. The "intraband" process corresponds to the coupling by the phonon of the spin-orbit split Λ_3 bands; it is characterized by the deformation potential, $d^5_{3,0}$.[10,11]

Information about the shape of the first-order Raman resonance of germanium near E_1, $E_1 + \Delta_1$ was obtained by Renucci *et al.*[12] prior to the availability of the cw dye laser. These authors shifted the $E_1 - E_1 + \Delta_1$ gaps of germanium to 2.37–2.55 eV by alloying with 22% of silicon, in order to bring

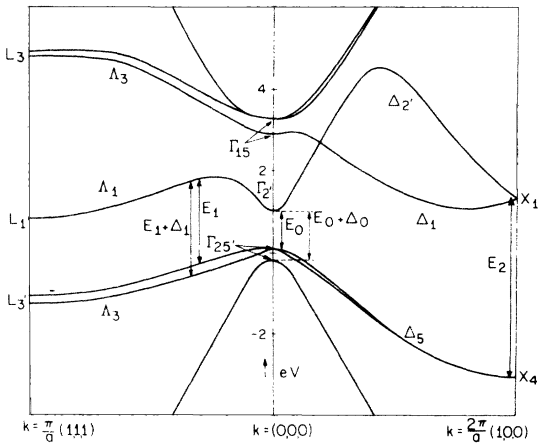

FIG. 1. Band structure of germanium showing the E_1 and $E_1+\Delta_1$, E_0, and $E_0+\Delta_0$ gaps. From Ref. 18.

them to the region where sufficient Ar^+-laser lines are available. Instead of separate resonances at E_1 and $E_1+\Delta_1$ they just saw one broad peak centered between the energies of these two gaps. Measurements with a cw dye laser[4] confirmed the line shape obtained by Renucci *et al.*[12] The absence of separate E_1, $E_1+\Delta_1$ resonances was then interpreted as due to the fact that the interband deformation potential for scattering by optical phonons is negligible compared with its intraband counterpart $d^5_{3,0}$. The intraband mechanism, i.e., the coupling by the phonon of the spin-orbit split valence bands, should produce a broad peak between the energies E_1 and $E_1+\Delta_1$, in agreement with the experimental observations.

The second-order Raman spectrum of germanium has been recently measured by Weinstein and Cardona[13] with a laser wavelength $\lambda = 5145$ Å (see Fig. 2). The Γ_1 component of this spectrum corresponds almost exclusively to overtone scattering and yields a fairly good picture of the density of *one-phonon* states (with the energy scale multiplied by two since these are overtone processes). The Γ_{12} component is only significant in the region of two optical phonons. Nevertheless, even in this region the Γ_{12} component with the Loudon normalization[14] ($|b|^2$) only amounts to one-tenth of the Γ_1 component $|a|^2$.[13] The $\Gamma_{25'}$ component ($|d|^2$ of the Loudon notation) amounts to 40% of $|a|^2$ in the two-optical-phonon region but is nearly negligible in the region of two TA overtones. A sharp peak appears at an energy equal to that of two optical phonons at Γ. This peak cannot be interpreted in terms of the density of overtone states. It was suggested[13] that this peak is due to iterative process (the first-order electron-phonon interaction taken in second-order perturbation theory) strongly resonant because of the vicinity of E_1, $E_1+\Delta_1$.

The experimental program discussed above leads to the measurement of the resonant behavior of the second-order Raman spectra of Ge (Γ_1 and $\Gamma_{25'}$ components; the Γ_{12} component is too small to be meaningfully studied). A preliminary measurement of the resonance of the linear combination of components $\Gamma_1+\Gamma_{12}+\Gamma_{25'}$ for the feature in Fig. 2 due to two TO phonons near L has been recently reported.[11] This linear combination is dominated

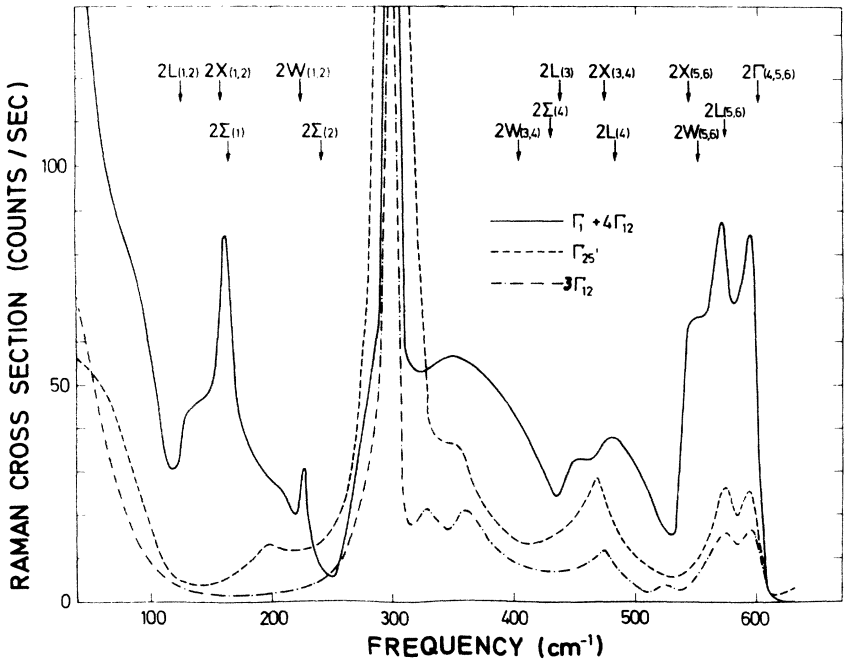

FIG. 2. Irreducible components of the first- and second-order Raman spectrum of germanium and assignment in terms of two-phonon critical points. The measurements, performed at room temperature for a laser wavelength $\lambda = 5145$ Å, are from Ref. 13.

by the Γ_1 component and, contrary to the $\Gamma_{25'}$ first-order resonance, it exhibits peaks near E_1 and $E_1 + \Delta_1$. Attempts to analyze these measurements theoretically were hampered by the fact that the resonance of the weak $\Gamma_{25'}$ component had not been measured and thus that of Γ_1 could not be completely isolated (the Γ_{12} component is negligible). In this paper, we present measurements of the resonance of the 2TO(L) structure of Fig. 2 near $E_1 - E_1 + \Delta_1$, as observed in the $\Gamma_{25'}$ component of the Raman spectrum. This resonance has the same shape as that of the first-order $\Gamma_{25'}$ phonon. This fact indicates that the two-phonon interband deformation potential D_1^5 is also negligible, a rather surprising result. From this $\Gamma_{25'}$ resonance we determine the corresponding two-phonon intraband deformation potential D_3^5. We use these results to extract the pure Γ_1 component of the 2TO(L) resonance from the $\Gamma_1 + \Gamma_{25'} + \Gamma_{12}$ combination ($\Gamma_{12} \simeq 0$) and the corresponding deformation potential D_1. We also present the $\Gamma_1 + \Gamma_{25'} + \Gamma_{12}$ resonance of the 2TO($W - X$) shoulder of Fig. 2 and that of the 2TA(X) structure. The latter resonance is essentially that of the pure Γ_1 component since the $\Gamma_{25'}$ and Γ_{12} components of the 2TA(X) scattering are negligible (see Fig. 2). We thus obtain from these data the D_1 deformation potential for scattering by two TA(X) phonons.

A detailed study of the resonance of the 2Γ optical phonon peak of Fig. 2 is also presented. It is shown that this peak is indeed only present near the resonant energies and thus resonates more strongly than all other two-phonon features. The position of the peak shifts slightly to lower frequencies with increasing laser frequency. All these peaks confirm the conjecture made earlier[11] that this resonance is an iterative effect of the first-order electron-phonon interaction.

THEORY

A. Processes (a) of Fig. 3

The theory of the resonant phenomena reported here is most easily presented in terms of the dielectric theory of Raman scattering.[8] This theory assumes that the frequency Ω of the excitation created in the Raman process is negligible compared with the relevant electronic energies, or, more precisely,

$$\Omega < |\omega - \omega_0 + i\eta| \ , \tag{1}$$

where ω is the laser frequency, ω_0 is the frequency of the resonant gap under consideration, and η is its lifetime broadening. Under these conditions the Raman tensor for first-order scattering R_{ij} can be written

$$R_{ij} \propto \frac{d\chi_{ij}}{d\xi} |\langle \xi^2 \rangle|^{1/2} \ , \tag{2}$$

where χ_{ij} is the electric susceptibility and ξ is the amplitude of the Raman phonon. For second-order scattering we must use instead of Eq. (2) the second derivative of χ multiplied by the average amplitudes of the two phonons involved. The cross section for Raman scattering is proportional to ω^4 multiplied by $|\vec{e}_i \cdot R \cdot \vec{e}_s|^2$, where $\vec{e}_i$ and $\vec{e}_s$ are the polarization vectors of the incident and the scattered field, respectively.

The derivative of Eq. (2) contains usually two distinct types of terms: terms due to phonon-induced variations in the energy gap between two bands (two-band terms) and terms produced by changes in the corresponding transition matrix elements. Matrix elements change due to changes in the wave functions produced by phonon-induced admixture of the two bands under consideration with a third band (three-band terms).

The theory of the changes in χ induced by perturbations of Γ_1, Γ_{12}, and $\Gamma_{25'}$ symmetry in the neighborhood of E_1, $E_1 + \Delta_1$ has been worked out in connection with the theory of piezoreflectance[15,16]; a hydrostatic stress has Γ_1 symmetry and pure shears along [100] and [111] have Γ_{12} and $\Gamma_{25'}$ symmetries, respectively. Hence, the differential expressions given in Refs. 15 and 16 apply to the first-order Raman tensor provided one replaces the strain deformation potentials d_1^5 and d_3^5 (the notation is that of Ref. 15) by the corresponding one-phonon deformation $\frac{1}{4}d_{1,0}^5$, $\frac{1}{4}d_{3,0}^5$ and the strain η_s by $4\xi/a\sqrt{3}$, where a is the lattice constant.[8,11] The component d_1 of the $\Gamma_{25'}$ first-order Raman tensor[14] thus becomes

$$d_1 = \left(\frac{2\sqrt{2}}{\sqrt{3}} \frac{\chi^+ - \chi^-}{\Delta_1} d_{3,0}^5 - \frac{1}{2\sqrt{3}} \frac{d\chi}{d\omega_1} d_{1,0}^5 \right) \frac{\langle \xi^2 \rangle^{1/2}}{a} \ , \tag{3}$$

where χ^+ and χ^- are the contribution to χ of E_1 and $E_1 + \Delta_1$, respectively. A different and independent derivation of Eq. (3) is given in the Appendix. The first term in brackets in Eq. (3) represents intravalley (three-band) contributions while the second term gives the intervalley (two-band) effects. The shape of these two contributions can be evaluated from the measured spectral dependence of the complex susceptibility χ.[17] This susceptibility can be split into E_1 and $E_1 + \Delta_1$ contributions χ^+ and χ^- in the manner suggested in Ref. 15. The derivative $d\chi/d\omega_1$ can be obtained by using the theoretical form of χ near E_1,[8]

$$\chi \propto \omega_1 \omega^{-2} f(\omega - \omega_1) \tag{4}$$

and similarly, around $E_1 + \Delta_1$ with ω_1 replaced by $\omega_1 + \Delta_1$. From Eq. (4) we find

$$\frac{d\chi}{d\omega_1} = -\frac{d\chi}{d\omega} + \chi \left(\frac{1}{\omega_1} - \frac{2}{\omega} \right) . \tag{5a}$$

Using the χ of Ref. 17 and Eq. (5) it is easy to see that for our purposes that

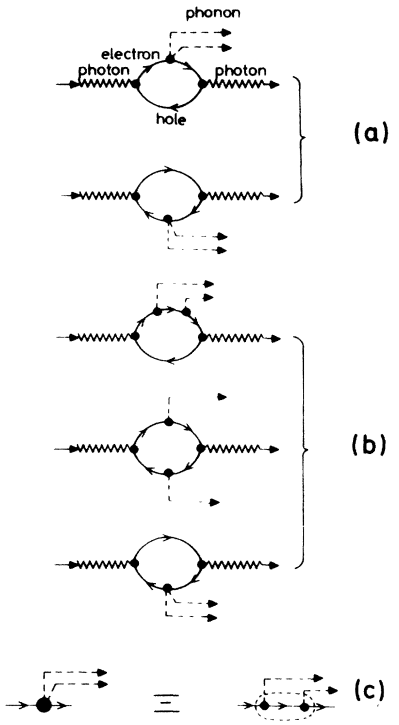

FIG. 3. Mechanisms which contribute to the two-phonon processes (a) electron–two-phonon interaction taken to first-order (b) electron–one-phonon interaction taken iteratively to second order. Diagram (c) shows how to include nonresonant-type (b) processes into those of type (a) by using a dressed electron-two-phonon vertex.

$$\frac{d\chi}{d\omega_1} \simeq -\frac{d\chi}{d\omega} \,. \tag{5b}$$

We nevertheless use here the complete expression for $d\chi/d\omega_1$ given in Eq. (5a).

Two distinct mechanisms contribute to two-phonon processes, as shown in Fig. 3. The processes of Fig. 3(a) are determined by the electron–two-phonon interaction vertices taken to first order while those of Fig. 3(b) represent iterative electron–one-phonon processes. As shown in Ref. 7 the separation into processes of types (a) and (b) is not unique: nonresonant and partly resonant processes of type (b) can be formally lumped together with type (a) processes by using a dressed interaction vertex as shown in Fig. 3(c).

Processes of type (a), with dressed interaction vertices, seem to dominate the second-order spectra of germanium-type materials. Since these processes have the same structure as the first-order processes (with the electron–two-phonon interaction), the corresponding Raman tensor can be obtained from the first-order expressions: the first-order deformation potential must be replaced by its electron–two-phonon counterpart and the phonon amplitude by the product of two-phonon amplitudes. The $\Gamma_{25'}$ component of the second-order spectrum thus becomes for a given pair of phonons [see Eq. (3)]:

$$d_2 = \frac{8}{\sqrt{3}}\left(\frac{\chi^+ - \chi^-}{\Delta_1} D_3^5 - \frac{1}{4\sqrt{2}} \frac{d\chi}{d\omega_1} D_1^5\right) \frac{\langle \xi_1^2 \rangle^{1/2} \langle \xi_2^2 \rangle^{1/2}}{a^2} \,, \tag{6}$$

where the electron–two-phonon deformation potential D_3^5 has been defined so as to have the coupling between the two split valence bands along $[11\bar{1}]$ produced by a phonon sublattice displacement of unit amplitude along [111] equal to

$$\frac{8}{3a^2} D_3^5 \,. \tag{7}$$

The Γ_{12} component of the second-order spectrum has only intraband (three-band) contributions near $E_1 - E_1 + \Delta_1$. It can be written as[11,15]

$$b_2 = \frac{8}{3} \frac{\chi^+ - \chi^-}{\Delta_1} D_3^3 \frac{\langle \xi_1^2 \rangle^{1/2} \langle \xi_2^2 \rangle^{1/2}}{a^2} \,. \tag{8}$$

Similarly, the Γ_1 component, containing only two-band terms[15] is

$$a_2 = \frac{4}{3} \frac{d\chi}{d\omega_1} D_1 \frac{\langle \xi_1^2 \rangle^{1/2} \langle \xi_2^2 \rangle^{1/2}}{a^2} \,. \tag{9}$$

Equations (3), (8), and (9) can be easily modified to take into account the finite frequency of the excitation Ω. This is done by replacing the derivatives $d\chi/d\omega$ by the finite differences

$$[\chi(\omega) - \chi(\omega - \Omega)]/\Omega \,, \tag{10}$$

where ω is the frequency of the incident laser, and by replacing $\chi^{\pm}$ by

$$\tfrac{1}{2}[\chi^{\pm}(\omega) + \chi^{\pm}(\omega - \Omega)] \,. \tag{11}$$

The constants D_3^5 and D_1^5 of Eq. (5) are, in principle, independent of each other. By making some simplifications about the structure of the Λ_1 conduction and Λ_3 valence functions it is possible, however, to find a relationship between D_3^5 and D_1^5. If we assume that the Λ_1 Bloch function (periodic part) is only an admixture of $\Gamma_{2'}$ and Γ_1 (s-like functions), the $\Gamma_{25'}$ phonons do not affect the Λ_1 state. To what extent this assumption is justified can be seen in Ref. 18. The Λ_1 state at the middle of the zone is about 60% Γ_1- and $\Gamma_{2'}$-like; the rest is mainly a $\Gamma_{25'}$ contribution from the valence bands which must make the approximation rather poor. Be it as it may, we pursue the path of this approximation and further assume that the Λ_3 bands have mainly $\Gamma_{25'}$ components at the top of the valence band. This approximation holds rather well, to about 80%.[18] Under these conditions one can prove that

$$d_{3,0}^5 = \sqrt{2}\, d_{1,0}^5 \,. \tag{12}$$

This relationship is completely general for all isomorphic deformation potentials such as D_3^5 and

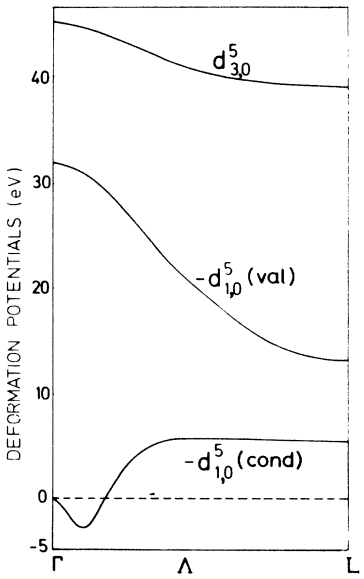

FIG. 4. Deformation potentials $d^5_{3,0}$, $d^5_{1,0}$ (cond), and $d^5_{1,0}$(val) as a function of k along the [111] direction of the Brillouin zone. *Note added in proof*: Due to an error in computations the values of $d^5_{1,0}$(cond) should be multiplied by 3.

D^5_1. Using this relationship one can estimate with Eq. (3) the relative contribution of intervalley and intravalley terms. Approximating the maximum of $d\chi/d\omega$ by χ/η, where η is the lifetime broadening of the structure, we find for the ratio of *intravalley*-to-*intervalley* Raman tensor components

$$d_{1,\text{intra}}/d_{1,\text{inter}} = 8(\eta/\Delta_1) \,. \tag{13}$$

For germanium $\eta \simeq 0.1$ eV, $\Delta_1 = 0.2$ eV and the $d_{1,\text{intra}}/d_{1,\text{inter}} \simeq 4$. This ratio makes the intervalley contribution small, but not negligible.

We have performed a pseudopotential calculation[8] of the variation of $d^5_{3,0}$ and $d^5_{1,0}$ with k along [111]. The results are shown in Fig. 4; $d^5_{1,0} = d^5_{1,0}(\text{cond}) - d^5_{1,0}(\text{val})$, where (cond) and (val) indicate the contribution of valence and conduction bands to $d^5_{1,0}$. Near Γ we have the relations

$$d^5_{3,0} = \sqrt{2}\, d_0 \,, \quad d^5_{1,0} = d_0 \,, \tag{14}$$

where d_0 is the deformation potential at Γ.[8] Deviations from Eq. (12) appear exclusively if there is significant admixture of $\Gamma_{12'}$ functions to the valence bands in the spirit of $\vec{k}\cdot\vec{p}$.[18] The coupling between the Γ_{15} and Γ_{12} components of the valence band produces the difference which, as shown in Fig. 4, has the effect of increasing drastically the ratio of Eq. (13). At the center of the Γ-L line the ratio of Eq. (13) becomes eight times larger since, according to Fig. 4, there is almost complete cancellation between $d^5_{1,0}$(val) and $d^5_{1,0}$(cond).

The dashed curve of Fig. 5 reproduces the experimental resonance of the Raman phonon of germanium.[4] The dashed-dotted and the solid curve are theoretical curves. The dashed-dotted line was obtained using for χ in Eq. (3) the experimental optical constants. The solid line was obtained, as discussed in the Appendix, from Eq. (A14), with the model density of states to be used later to calculate iterative processes [Fig. 2(b)] and the average deformation potentials $d^5_{1,0}(\text{cond}) = -5$ eV, $d^5_{1,0}(\text{val}) = -17$ eV, $d^5_{3,0} = 40$ eV, taken from Fig. 5.

B. Iterative processes (b) of Fig. 3

The diagram in Fig. 3(b) is obtained in fourth-order perturbation theory whereas that in Fig. 3(a) is obtained in third-order perturbation theory. Correspondingly, the analytic expression for Fig. 3(b) has one energy denominator more than that of Fig. 3(a). For all intermediate states for which this additional energy denominator is large, diagram 3(b) can be added to diagram 3(a), thus renormalizing the electron–two-phonon interaction. This is illustrated in Fig. 3(c). For some intermediate states, all the energy denominators of Fig. 3(b) can become small leading to a strong enhancement in the scattering cross section. The iterated process [Fig. 3(b)] therefore should contain contributions which resonate more strongly than those of Fig. 3(a). This will hold if enough intermediate states are available which lead to three resonant energy denominators, that is, near interband critical points, especially when there are indirect gaps nearby.[19] These relevant intermediate states only extend over a small portion of the Brillouin zone. If no indirect gaps are involved, only small momentum transfer to phonons occurs if the strongest resonance condition is obeyed. Thus, this type of Fig. 3(b) process involves only near-zone center phonons. The observed Raman

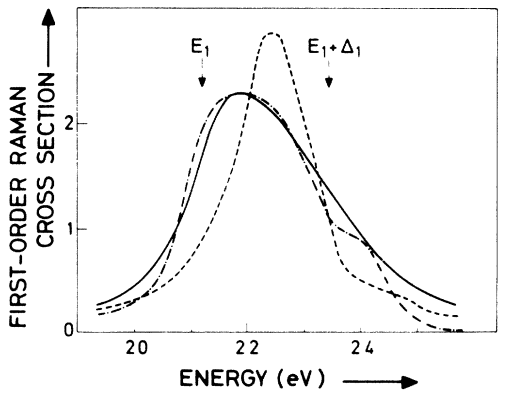

FIG. 5. Experimental resonance observed for the one-phonon Raman scattering in germanium (dashed curve). The dash-dotted line was calculated from experimental values of the optical constants with Eq. (3) for $d^5_{1,0} = 0$ (Ref. 4). The solid line was obtained from Eq. (A12) with $d^5_{1,0}(\text{cond}) = -5$ eV, $d^5_{1,0}(\text{val}) = -17$ eV, $d^5_{3,0} = 40$ eV and with the model bands used in this paper.

peaks are "anomalous" in that they do not correspond to peaks in the joint density of states (in fact the density of states vanishes where these peaks appear).

Another peculiarity of the diagram of Fig. 3(b) is that the additional energy denominator [compared to diagram 3(a)] contains the transferred momentum which determines the kinetic energy of the intermediate electron-hole pair. The momentum integration over final phonons affects the resonance behavior of this energy denominator and weakens the resonance. On the other hand, the kinetic energy of the electron-hole pair can make the energy denominator vanish for a finite momentum even if the laser frequency is above the critical point. The higher the incident frequency above the critical point, the bigger the momentum of phonons will have to be for which the energy denominator becomes resonant. This leads to a shift of the anomalous peak to lower wave numbers with increasing incident frequency above the critical point.[20]

Unlike the diagram of Fig. 3(a), diagram of Fig. 3(b) cannot be represented as a derivative of linear susceptibilities and must be calculated directly using a definite model for the relevant energy bands.[21] In our case a three-band model is appropriate. Diagram 3(b) then leads to the following analytic expression for the Raman tensor:

$$
\begin{aligned}
&R_{\gamma\gamma'}(Q, j_1 j_2) \\
&= \sum_{v v' v''}^{\vec{p}} g_v^*(\vec{p}, \gamma)\{[f(\vec{p}, \vec{Q} j_1)\delta_{vv'} - f_{vv'}(\vec{p}, \vec{Q} j_1)][f(\vec{p}, -\vec{Q} j_2)\delta_{v'v''} - f_{v'v''}(\vec{p}, -\vec{Q} j_2)] + (\vec{Q} j_1) \longleftrightarrow (-\vec{Q} j_2)\} g_{v'v''}(\vec{p} + \{\vec{0}\}) \\
&\times [\hbar\omega + i\eta - \hbar\omega_c(\vec{p}) + \hbar\omega_v(\vec{p})]^{-1} \; [\hbar\omega + i\eta - \hbar\Omega_{j_1}(\vec{Q}) - \hbar\omega_c(\vec{p} + \{\vec{0}\}) + \hbar\omega_{v'}(\vec{p} + \{\vec{0}\})]^{-1} \\
&\times [\hbar\omega + i\eta - \hbar\Omega_{j_1}(\vec{Q}) - \hbar\Omega_{j_2}(\vec{Q}) - \hbar\omega_c(\vec{p} + \{\vec{0}\}) + \hbar\omega_{v''}(\vec{p} + \{\vec{0}\})]^{-1} \; . \qquad (15)
\end{aligned}
$$

The coupling functions f and g are defined in Eqs. (A1), (A10), and (A11). In the second energy denominator of Eq. (15) $\hbar\omega_c(\vec{p}+\vec{Q})$ and $\hbar\omega_{v'}(\vec{p})$ must be taken if electron scattering is considered. Similarly $\hbar\omega_c(\vec{p})$ and $\hbar\omega_{v'}(\vec{p}+\vec{Q})$ must be taken for hole scattering. In the third energy denominator and the coupling function $g_{v'v''}$, the argument $\vec{p}+\vec{Q}$ has to be used if both the electron and the hole are scattered during the whole process, otherwise use the argument $\vec{p}$.

The different contributions of expression (15) are illustrated in Fig. 6. Figures 6(a)–6(c) describe iterated hole scattering, Fig. 6(d) iterated electron scattering and Figs. 6(e) and 6(f) mixed electron-hole scattering. Assuming, as we did in the previous section, that the $\Gamma_{25'}$ optical phonon does not affect the conduction band Λ_1 (that $d^5_{1,0}$(cond) is small) processes (d)–(f) can be neglected. Also, if the two-band terms are negligible with respect to the three-band terms like in first-order scattering, we are left with only Fig. 6(a).[11] These approximations give a simple, physical model and lead to good agreement with experiment as will be shown below. For Fig. 6(a), Eq. (15) simplifies to

$$
\begin{aligned}
T^{(1)}_{\gamma\gamma'}(\vec{Q}, j_1 j_2) &= \sum_{v \neq v'}^{\vec{p}\,'} g_v^*(\vec{p}, \gamma)[f_{vv'}(\vec{p}, \vec{Q} j_1) f_{v'v}(\vec{p}, -\vec{Q} j_2) + f_{vv'}(\vec{p}, -\vec{Q} j_2) f_{v'v}(\vec{p}, \vec{Q} j_1)] g_v(\vec{p}, \gamma') \\
&\times [\hbar\omega + i\eta - \hbar\omega_c(\vec{p}) + \hbar\omega_v(\vec{p})][\hbar\omega + i\eta - \hbar\Omega_{j_1}(\vec{Q}) - \hbar\omega_c(\vec{p}) + \hbar\omega_{v'}(\vec{p}+\vec{Q})] \qquad (16) \\
&\times [\hbar\omega + i\eta - \hbar\Omega_{j_1}(\vec{Q}) - \hbar\Omega_{j_2}(\vec{Q}) - \hbar\omega_c(\vec{p}) + \hbar\omega_v(\vec{p})] \; , \\
R_{\gamma\gamma'}(\vec{Q}, j_1 j_2) &= \sum_{l=1}^{8} T^{(l)}_{\gamma\gamma'}(\vec{Q}, j_1 j_2) \; .
\end{aligned}
$$

In Eq. (16) the $\vec{p}$ sum has been split into a l sum over the eight valleys along the unit vector $\vec{e} = (\pm 1, \pm 1, \pm 1)/\sqrt{3}$ and a restricted $\vec{p}$ sum over the corresponding valley. Using a critical-point analysis the matrix elements are assumed to be independent of momentum. Using symmetry operations (for instance, the inversion and rotation by π) the contributions of the different valleys can be transformed into those of a standard valley. The combinations $(\gamma\gamma' j_1 j_2) = (xxxx), (xxyy), (xyxy)$ in $T^{(l)}_{\gamma\gamma'}(\vec{Q}, j_1 j_2)$ plus all symmetry related combinations transform like the identity and lead to a construc-

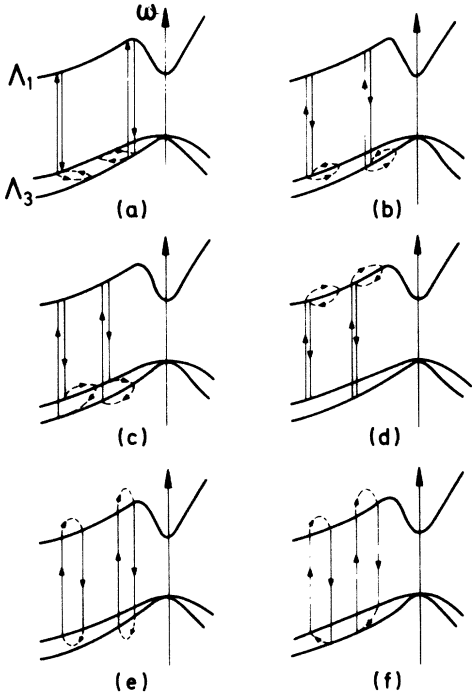

FIG. 6. Schematic representation of the various terms which contribute to Eq. (15) for the E_1, $E_1+\Delta_1$ gaps.

tive valley summation. These are the terms we shall only consider in the following. We have calculated the ones which lead to a destructive l sum and found that their contributions were two orders of magnitude smaller. Using Eq. (A1), (A10), and (A11) the absolute square of the transition matrix element can then be written

$$|R_{\gamma\gamma'}(\vec{Q}, j_1 j_2)|^2 = 4|M_{\gamma\gamma' j_1 j_2}|^2 \left| \sum_{\substack{v\neq v' \\ l=1,4}} S_{vv'v}(Q_l) \right|^2 , \quad (17)$$

with

$$M_{\gamma\gamma' j_1 j_2} = 2\,\mathrm{Re}\{g_1^*(\gamma)[f_{12}(j_1)f_{21}(j_2) + f_{12}(j_2)f_{21}(j_1)]g_1(\gamma')\} . \quad (18)$$

Here we used the fact that opposite valleys are equivalent giving a prefactor 4 restricting the l sum to four terms. S denotes the sum over the three energy denominators; Re means the real part. Neglecting the $\vec{Q}$ dependence of the phonons, S depends only on the projected momentum $Q_l = |Q|\{1-[(Q/|\vec{Q}|)\cdot\vec{e}_l]^2\}^{1/2}$, $l=1,2,3,4$ within the effective-mass approximation for the critical points E_1 and $E_1+\Delta_1$.

The symmetry properties of the cross section solely come from the quantity $M_{\gamma\gamma' j_1 j_2}$. Using Eqs. (A1), (A10), and (A11) we easily verify the relations $M_{xxxx} = M_{xxyy} = M_{yyxx} = 4M_{xyxy}$. From that follows, for the different symmetry components of the cross section,

$$\left(\frac{d\sigma}{d\Omega}\right)^{\Gamma_{25'}} = \frac{1}{6}\left(\frac{d\sigma}{d\Omega}\right)^{\Gamma_1} , \quad (19)$$

$$\left(\frac{d\sigma}{d\Omega}\right)^{\Gamma_{12}} = 0 . \quad (20)$$

It is difficult to check the predictions of Eqs. (19) and (20) with the presently available experiment data. Figure 2, however, supports qualitatively relations (19) and (20).

The frequency dependence of the cross section comes solely from the S terms in Eq. (17). Let us introduce the following abbreviations:

$$\alpha_v^{(n)} = \frac{\hbar\omega + i\eta - n\hbar\Omega - \epsilon_v}{\epsilon} , \qquad v=1,2, \quad n=0,1,2, \quad \epsilon = \frac{\hbar^2}{2\mu a^2} . \quad (21)$$

In Eqs. (20) and (21) μ is the reduced mass which is the same for both valence bands, a is the lattice constant and ϵ_1, ϵ_2 are the energy gaps E_1 and $E_1+\Delta_1$. Using an effective mass approximation for the band energies around the E_1 and $E_1+\Delta_1$ critical points are neglecting the linear terms, one obtains

$$S_{vv'v}(Q) = \frac{\sqrt{3}\pi C}{a}\frac{1}{\epsilon^3}\frac{V^{1/3}}{2\pi} \times \sum_{\vec{p}_\perp}[(\alpha_{cv}^{(0)} - \vec{p}_\perp^{\,2}a^2)(\alpha_{cv}^{(2)} - \vec{p}_\perp^{\,2}a^2)]^{-1} \times \left(\alpha_{cv'}^{(1)} - \frac{\mu}{m_h}(Qa)^2 - \vec{p}_\perp^{\,2}a^2 - 2\frac{\mu}{m_h}a\vec{p}_\perp\cdot Qa\right)^{-1} . \quad (22)$$

In Eq. (22) we have carried out the longitudinal $\vec{p}$ sum parallel to $(1,1,1)/\sqrt{3}$ which gives $3\pi C/a$, where C is a cutoff factor $\simeq \frac{2}{3}$.[8] The transverse sum $\sum_{\vec{p}_\perp}$ can be carried out in cylindrical coordinates and one obtains for $\omega < \epsilon_1$,

$$S_{vv'v}(Q) = \frac{\sqrt{3}CV}{8\pi a^3\epsilon^2\hbar\Omega}\left[I\left(-\alpha_v^{(2)}, -\alpha_{v'}^{(1)} + \frac{\mu}{m_h}(Qa)^2 - \frac{2\mu^2}{m_h^2}(Qa)^2, \alpha_{v'}^{(1)} - \frac{\mu}{m_h}(Qa)^2\right) - I\left(-\alpha_v^{(0)}, -\alpha_{v'}^{(1)} + (Qa)^2\frac{\mu}{m_h}\left(1-2\frac{\mu}{m_h}\right), \alpha_{v'}^{(1)} - \frac{\mu}{m_h}(Qa)^2\right)\right] , \quad (23)$$

where m_h is the hole mass and I is the integral

$$I(\beta, b, c) = \int_0^\infty dx \frac{1}{x+\beta}\frac{1}{(x^2+2bx+c^2)^{1/2}} = \frac{1}{\gamma}\ln\left(\frac{\gamma c + c^2 - \beta b}{\beta(\gamma + b - \beta)}\right) , \quad (24)$$

with $\gamma = (\beta^2 - 2b\beta + c)^{1/2}$.

The function S is obtained for $\omega > \omega_1$ from Eqs. (23) and (24) by analytic continuation. Taking all equations together one obtains for the component Γ_1 the following cross section:

$$\left(\frac{d\sigma}{d\Omega}\right)^{\Gamma_1} = \frac{9\omega'^2 |g|^4 (d_{3,0}^5)^4}{2(2\pi)^5 a c^4 V M^2 \Omega^2} \times \int_0^D dX X^2 \int d\Omega \left| \sum_{\substack{v \neq v' \\ l=1,4}} S_{vv'v}(X_l) \right|^2 . \quad (25)$$

D is a cutoff for the final momentum integration of the order 1. X_l is defined as $Q_l a$ and M is the mass of the nucleus.

EXPERIMENTS

The experiments reported here were performed at room temperature in the backscattering configuration. The sample was cut out of an ingot of n-type germanium of 30-Ω cm resistivity. All measurements were performed on a (100) face, x-ray oriented to ± 2°, polished-etched with Syton. The pure $\Gamma_{25'}$ component of the spectrum (d_2) was observed for incident and scattered polarizations parallel to [010] and [001], respectively. The sum of the Γ_1, $\Gamma_{25'}$, and Γ_{12} components was observed for both polarizations parallel to [110].

The measurements were taken with a 1m Spex double monochromator outfitted with a triple monochromator. Detection was performed with an RCA C31034 multiplier by photon counting with a multichannel counter swept as a function of wavelength. A 165 Spectra Physics Kr-ion and a Spectra Physics model No. 170 (24 W in all lines) Ar-ion laser were used to provide discrete wavelengths. Continuously tunable wavelengths were obtained with a Rhodamine SiC 6G-run Spectra Physics model No. 370 cw dye laser. This laser was also operated with a Rhodamine 6G solution in water and hexafluoroisopropanol (1:1). The laser radiation was focused on the sample with a cylindrical lens (image parallel to monochromator slit). This procedure was of particular importance to avoid heating since laser powers as high as several watts were sometimes used.

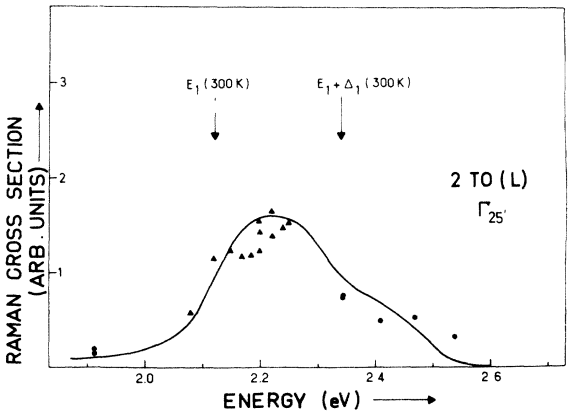

FIG. 8. Resonance of the 2TO(L) peak of the two-phonon spectrum of germanium in the $\Gamma_{25'}$ configuration. Circles: gas laser lines; triangles: tunable dye laser. The solid curve is obtained with Eq. (6) with $D_1^5 \simeq 0$.

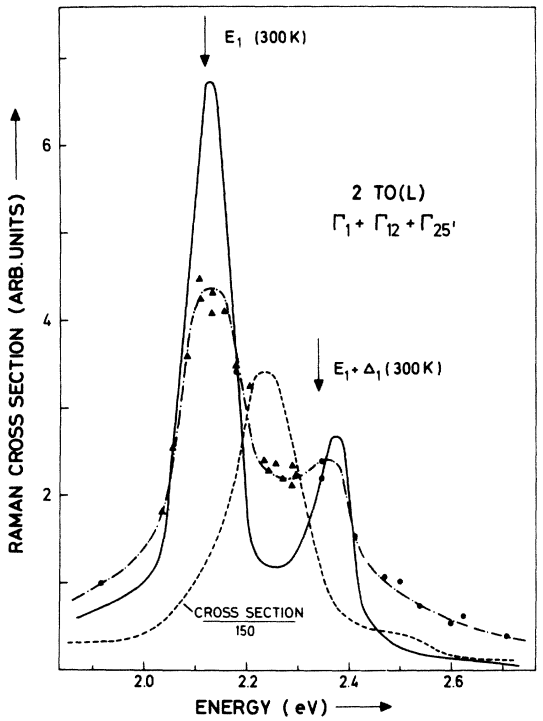

FIG. 7. Resonance of the 2TO(L) Raman peak of germanium near the E_1 and $E_1+\Delta_1$ peaks. The circles and triangles represent points taken with ion lasers and tunable dye lasers, respectively. The dashed line represents the resonance of the first-order spectrum. The vertical scale represents the height of the observed peaks in arbitrary units which, nevertheless, are the same in this and all subsequent second-order resonance curves. The first order heights have been divided by 150. The solid line is a theoretical curve for the second-order spectrum obtained as described in the text. All measurements were made at room temperature. In order to bring the experimental and the theoretical curves to coincide, the latter has been shifted by 20 meV.

RESULTS AND DISCUSSION

A. Resonances due to electron-two-phonon interaction

The points in Fig. 7 show the resonance in the $\Gamma_1 + \Gamma_{25'} + \Gamma_{12}$ 2TO(L) phonon of germanium discussed already in Ref. 11. The dashed line is the resonance of the first-order phonon reported in Ref. 4. This resonance, peaked between E_1 and $E_1+\Delta_1$, differs rather drastically from the second-order resonance which exhibits distinct peaks slightly above E_1 and $E_1+\Delta_1$, respectively. The solid line is an attempt at fitting the experimental

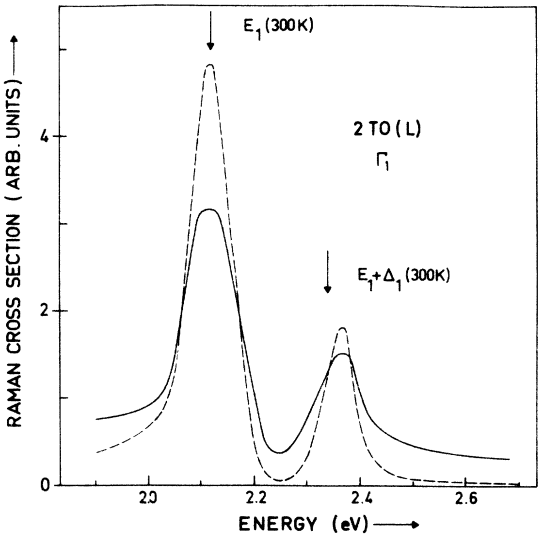

FIG. 9. Experimentally obtained resonance of the Γ_1 component of the 2TO(L) Raman spectrum of Ge (see text). The dashed line was obtained with Eq. (9) with the derivative replaced by the finite difference of Eq. (9) and shifted by 17 meV to higher energies.

points with a sum of Γ_1 [Eq. (9)], Γ_{12} [Eq. (8)], and $\Gamma_{25'}$ [Eq. (6) with $D_1^5 \simeq 0$] contributions. The theoretical curve was obtained by using finite differences instead of derivatives [Eqs. (10) and (11)] and, for a better fit, had to be shifted by 20 meV to higher energies. Shifts of this magnitude are required in many resonant Raman experiments, especially those around E_1 and $E_1 + \Delta_1$.[22]

Figure 8 shows the resonance in the $\Gamma_{25'}$ component of the 2TO(L) peak of Fig. 2. A comparison with Fig. 7 shows that this resonance is very different from the Γ_1 resonance and rather similar to the $\Gamma_{25'}$ first-order resonance. The solid curve in Fig. 7 was obtained with Eq. (6) using the optical constants of Ref. 17 for $D_1^5 \simeq 0$, with a shift of 37 meV to higher energies. The accidental but simultaneous cancellation of the first-order ($d_{1,0}^5$) and the second-order (D_1^5) deformation potentials is indeed quite remarkable.

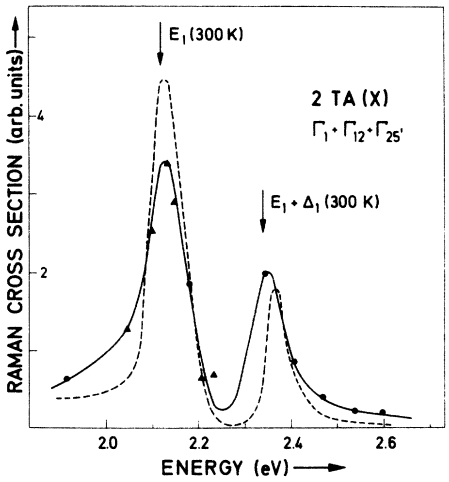

FIG. 10. Experimentally obtained resonance of the $\Gamma_1 + \Gamma_{25'} + \Gamma_{12}$ components of the 2TA(X) peak of Fig. 2. The triangles are dye laser points; the circles gas laser points. The dashed line was obtained with Eq. (10) shifted by 66 meV to higher energies.

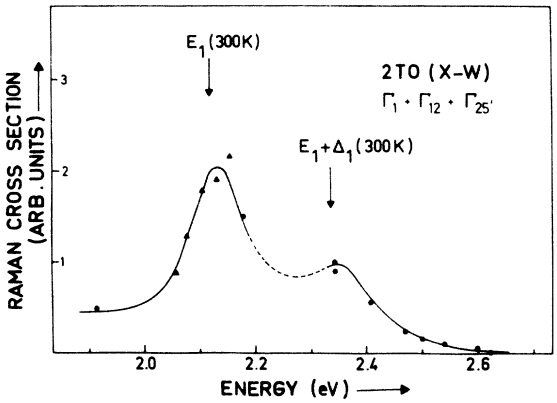

FIG. 11. Experimentally obtained resonance of the $\Gamma_1 + \Gamma_{25'} + \Gamma_{12}$ components of the 2TO($X - W$) peaks of the Raman spectrum of germanium (Fig. 2). The triangles are dye laser points, the circles gas laser points.

Using the results of Fig. 8 it is possible to extract from Fig. 7 the shape of the separate Γ_1 resonance. Under the assumption $D_1^5 \simeq 0$, the $\Gamma_{25'}$ and Γ_{12} resonances have the same shape [Eqs. (6) and (8)]. From Ref. 7 we find $b_2^2 \simeq \frac{1}{4} d_2^2$ at 5145 Å. Since the shapes of both resonances are the same we assume this relationship to hold throughout the whole spectrum. Hence, the Γ_1 component is found by subtracting from the measurements of Fig. 7, $\frac{5}{4}$ of those of Fig. 8. The results are shown by the solid line of Fig. 9. The dashed line was obtained from Eq. (9) with the derivative replaced by the finite difference of Eq. (10) using the optical constants of Ref. 17.

We show in Fig. 10 the resonance of the $\Gamma_1 + \Gamma_{25'} + \Gamma_{12}$ component of the 2TA feature in the acoustical part of the two-phonon spectrum of germanium. Since according to Fig. 2 for this structure $\Gamma_{25'} \simeq \Gamma_{12} \simeq 0$, the points of Fig. 10 should represent the pure Γ_1 component. The fit to the theoretical curve [Eq. (9) shifted by 66 meV to higher energies] is reasonably good.

For the sake of completeness we show in Fig. 11 the height of the 2TO($X - W$) structure of Fig. 2 (see also Fig. 12). This resonance is rather similar in shape to the 2TO(L) resonance of Fig. 7. Since we have not measured the $\Gamma_{25'}$ component of the resonance of Fig. 11, we cannot extract the Γ_1

TABLE I. Energies (in meV) by which one must shift the calculated resonance curves of germanium in order to agree with experiment. A shift of 40 meV was also needed for the first-order scattering of InSb near E_1 $-E_1+\Delta_1$ (Ref. 22).

	2TA(X)	2TO(L)
Γ_1	66	17
$\Gamma_{25'}$		37

component. Figure 12 shows the complete 2TO spectrum ($\Gamma_1+\Gamma_{12}+\Gamma_{25'}$) for several laser wavelengths.

The theoretical curves of Figs. 7–11 had to be slightly shifted to higher energies to represent the experimental data. These shifts are presented in Table I. For the $E_1-E_1+\Delta_1$ first-order resonance of InSb a similar shift (40 meV) is required. These shifts have a sign opposite to that which would be required if it were due to laser heating. It has also been pointed out[12] that the shift with temperature of the electronic critical energies (i.e., peaks) observed in the Raman resonances is smaller than that found from the optical spectra. Thus, the discrepancy between "Raman" and optical gaps increases with increasing temperature. Similar discrepancies (~0.15 eV) have also been found for the E_0 resonance of some of the second-order Raman peaks of GaP,[7,26] although the first-order peak seems to resonate at the same energy as the optical constants.[6] It is nevertheless more difficult to establish these shifts near E_0 than near E_1 because of the large corrections which have to be applied to the experimental data in order to take into account the rapidly varying absorption coefficient.

A satisfactory theoretical account of these shifts has yet to be given. The correspondingly small temperature shift of the Raman gaps suggests that it may be related to the negative contribution to the low-temperature gaps produced by the self-energy of the zero-point phonons. This shift or "dressing" of the electronic gaps should be fully present in the optical spectra. For a reason not clear to the authors, the Raman spectra may be sampling a less dressed gap.

B. Deformation potentials for electron-two-phonon interaction

From the theoretical fits to the curves of Figs. 8–10 it is possible to determine the deformation potentials D_3^5 and D_1 for 2TO(L) scattering and D_1 for 2TA(X) scattering by comparison with the first-order results of Fig. 7, provided $d_{3,0}^5$ is known. We must point out, however, that the vertical scales of Figs. 7–10 represent measured peak heights. In order to determine deformation potentials we need ratios of total scattering intensities, i.e., ratios of areas under the Raman spectra. The ratios of heights were normalized into ratios of areas by using the ratios of areas measured at 2.18 eV and given in Table II. We take for the area of the TO and TA second-order spectra the total area of these branches and not only that of the critical point since it is not possible to separate exactly the critical point from the remaining contributions of the phonon branch. It is, however, clear that this intensity, and thus the calculated deformation potentials, must be determined by the contribution of the most prominent critical point (X for TA, L for TO).

The deformation potential $d_{3,0}^5$ should be the average for all the region of $\vec{k}$ space involved in the transitions; the averaging is made easier by the fact that $d_{3,0}^5$ is nearly constant in the Γ-L region (see Fig. 4). We take $d_{3,0}^5=40$ eV, the value at the center of the Γ-L region. In Ref. 11 we had used $d_{3,0}^5=15.4$ eV, the value calculated for *silicon* at the L point by Goroff and Kleinman.[23] Since the structure and eigenvectors of the top valence band is nearly the same for silicon as for germanium[18] we would expect $d_{3,0}^5$ also to be nearly the same. We do not, at present, understand the reason for the discrepancy.

For the Γ_1 overtone resonances we have from Eqs. (3) and (9)

$$\frac{I_2(\Gamma_1)}{I_1(\Gamma_{25'})}=\left|\frac{\Delta_1}{a\sqrt{6}}\frac{1+n_B(\omega_2)}{[1+n_B(\omega_1)]^{1/2}}\times\left(\frac{d\chi}{d\omega_1}\Big/\chi^+(\omega)-\chi^-(\omega)\right)\left(\frac{\hbar}{4M}\right)^{1/2}\frac{\sqrt{\omega_1}}{\omega_2}\frac{D_1}{d_{3,0}^5}\right|^2, \tag{26}$$

where M is the atomic mass, ω_1 is the first-order Raman frequency, ω_2 is the second-order phonons and n_B is the Raman frequency of the Bose-Einstein factor. The functions $d\chi/d\omega_1$ (actually the ratio of finite differences mentioned earlier) and $\chi^+-\chi^-$ are shifted so as to obtain the best fit to the experimental data.

For the $\Gamma_{25'}$ second-order contribution we find from Eqs. (3) and (6)

$$\frac{I_2(\Gamma_{25'})}{I_1(\Gamma_{25'})}=\left|\frac{2\sqrt{2}}{a}\frac{1+n_B(\omega)}{[1+n_B(\omega_1)]^{1/2}}\frac{(\chi^+-\chi^-)_2}{(\chi^+-\chi^-)_1}\times\frac{\hbar}{4M}\frac{\omega_1}{\omega_2}\frac{D_3^5}{d_{3,0}^5}\right|^2. \tag{27}$$

The deformation potentials calculated with Eqs. (26)

TABLE II. Ratios of second- to first-order scattering intensities at 2.18 eV.

	Γ_1	$\Gamma_{25'}$
2TO	0.048	0.025
2TA	0.028	

TABLE III. Deformation potentials calculated with Eqs. (26) and (27) in eV for TO and TA phonons in Ge at the E_1 gap. Also shown are the analogous deformation potentials found for the E_0 edge of GaP and ZnTe.

		D_1	D_3^5, D_{15}	D_1^5	D_3^3
Ge(E_1)	2TO	2534	543	0	470
	2TA	170	0	0	0
GaP(E_0)[a]	2TO	1670	...	...	...
	2LO	2180	...	...	...
	TO+LO	...	450	...	...
	2TA	675	...	...	...
ZnTe(E_0)[b]	2TA	675	...	...	...
	2LO	0	...	...	...
	TA+LO	...	400	...	...
	TO+LO	...	115	...	...
InSb(E_0)[c]	2TA	15000			
	2TO	620			

[a]From Ref. 7.
[b]R. Schmidt, B. McCombe, and M. Cardona (unpublished).
[c]K. L. Ngai and A. K. Ganguly, Proceedings of the NATO Summer Institute, Antwerp 1973 (unpublished); also K. L. Ngai (private communication).

and (27) for the TO and TA phonons are listed in Table III together with the analogous deformation potentials (D_1, D_{15}) found for the E_0 edge of GaP, ZnTe, and InSb. The deformation potential for the Γ_{12} component of the 2TO phonons D_3^3 was obtained without measuring the resonance, from the ratio of this component to the first-order line determined at 2.41 eV in Ref. 7.

Concerning the 2TO deformation potentials, we note a decrease from Ge to GaP and a very rapid decrease to near zero from GaP to ZnTe. The 2TA deformation potential increases from Ge to the polar materials. We do not know at present whether they are complicated by the different nature of the resonances observed for germanium (E_1, $E_1+\Delta_1$) and for the polar compounds (E_0, $E_0+\Delta_0$). We are measuring at present E_1, $E_1+\Delta_1$ resonances in InSb and GaSb in order to ascertain this point and to obtain a clear pattern of the systematics of electron–two-phonon deformation potentials.

C. Resonances due to iterated electron-one-phonon interaction

The second-order Raman spectrum of germanium in the 2TO region is shown in Fig. 12 for five different laser wavelengths covering the E_1, $E_1+\Delta_1$ region. We note a change in the shape of this spectrum with laser wavelength involving mainly a stronger resonance of the 2TO(Γ) feature (which peaks about 2.4 eV). The 2TO(Γ) peak shifts to lower wave numbers with increasing laser frequency. Both the strong resonance and the shift to

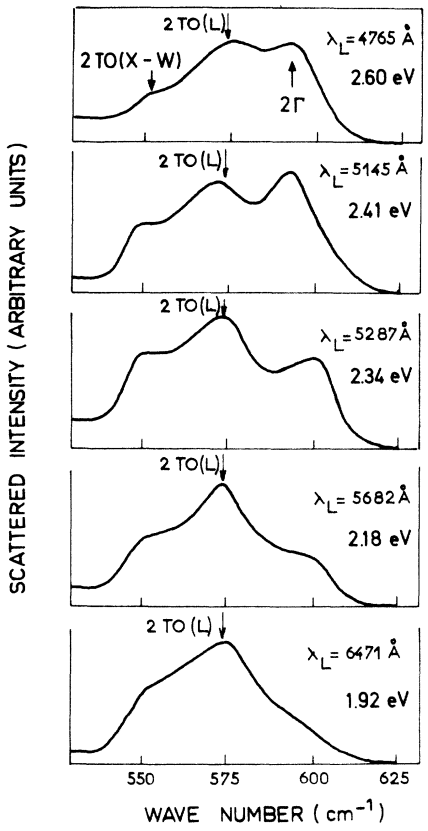

FIG. 12. $\Gamma_1+\Gamma_{12}+\Gamma_{25'}$ component of the second-order Raman spectrum in the region of overtone scattering by 2TO phonons for five different laser wavelengths.

smaller wave numbers are characteristic of processes of the type of Fig. 3(b) and Eq. (15). As discussed in the previous subsection for the $E_1-E_1+\Delta_1$ gaps these processes are mainly of the form of Fig. 6(a). We plot in Fig. 13 the strengths of

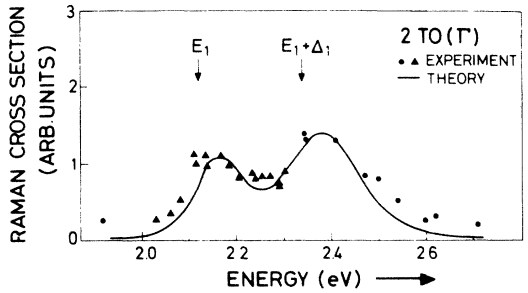

FIG. 13. Resonance of the Γ_1 component of the 2TO(Γ) structure of Fig. 12. We have plotted the areas of the structure obtained by subtraction of the low-energy curve [Fig. 10, $\omega=1.92$ eV] from the curve at the laser energy of the horizontal scale. Triangles: dye-laser points; circles: gas laser. Solid curve: theory calculated with the damping constants $\eta_1=1.3\hbar\Omega_{TO}$ and $\eta_2=2.8\ \hbar\Omega_{TO}$ for the E_1 and $E_1+\Delta_1$ gaps, respectively and the masses $m_{e\perp}=0.082m$, $m_h=0.22m$.

the 2Γ optical resonance as a function of phonon energy. We have also plotted in this figure the calculated cross-section for 2TO(Γ) scattering using Eq. (25) together with experimental points. A cutoff D of one and damping constants $\eta_1 = 1.3\hbar\Omega_{TO}$ and $\eta_2 = 2.8\hbar\Omega_{TO}$ for the E_1 and $E_1 + \Delta_1$ gaps were chosen. The other band parameters were taken from Ref. 8. The calculated curve does not depend very much on the value chosen for D. The choice of the damping constants was determined by two conditions: (a) the shape of the 1TO resonance, calculated with Eq. (A14), should reproduce reasonably well the experiments. Figure 5 shows that the calculated first-order cross section using the above damping constants agrees with the absolute square of the derivative of the experimental linear susceptibility. This ensures that our band model for the E_1 and $E_1 + \Delta_1$ gaps is realistic; (b) the ratio of the $E_1 + \Delta_1$ peak to the E_1 peak depends sensitively on the ratio η_2/η_1. Using the same damping for both gaps would enhance the $E_1 + \Delta_1$ maximum by one order of magnitude compared to the E_1 maximum, contrary to observations. A damping η_2 larger than η_1 is reasonable because the $E_1 + \Delta_1$ gap lies in the continuum of the E_1 states and is thus affected by more elastic scattering channels. Modulation spectroscopy for many germanium and zinc-blende-type materials, suggest $\eta_2 \simeq 1.5\ \eta_1$.[24]

Using Eqs. (25) and (A14), together with the calculated deformation potential, a theoretical ratio of about 0.01 is obtained for 2TO(Γ) to 1TO(Γ) scattering. The experimental ratio is of this order of magnitude, a rather direct proof that the 2TO(Γ) structure is indeed due to iterated first-order processes. The theoretical and experimental frequency dependence in Fig. 13 agree quite well. There are some discrepancies for the high- and low-frequency wings which, however, could be due to the procedure used to isolate the 2TO(Γ) structure from the less resonant background.

Figure 14 shows the quantity $|\sum_{v \neq v'} S_{vv'v}(X)|^2$, calculated only for one valley, as a function of the transverse momentum $X = aQ$. This quantity indicates whether only a small region around the $\langle 1, 1, 1\rangle$ axes contributes effectively to the 2TO(Γ) scattering or whether an extended Brillouin zone region contributes. The solid curve calculated for an incident frequency $\hbar\omega = E_1 - 3.5\ \hbar\Omega_{TO}$ falls off only slowly with increasing X; thus, for this frequency nearly all phonons in the Brillouin zone contribute. This case does not lead to a well defined 2TO(Γ) structure: The 2TO(Γ) iterative peak becomes broad and vanishes rapidly for long wavelengths. At these frequencies, peaks in the two-phonon density of states dominate the second order spectrum.

At higher frequencies the region which contributes effectively to the sum over final states narrows and leads, for energies $\hbar\omega \gtrsim E_1 + \Delta_1$, to a sharp peak which shifts to higher transverse momentum with increasing incident frequency. The origin of the shift is clear: When the incident frequency is above the gap the additional energy denominator of the iterated process becomes resonant for finite momentum of the recoil kinetic energy of the electron-hole pair. The higher the incident frequency, the larger must be the momentum to make the energy denominator resonant. From Fig. 14 the following qualitative predictions can be made: If $\hbar\omega \ll E_1$ the 2TO(Γ) iterative contribution should grow out of the background with increasing frequency as a broad structure. For $\hbar\omega \gtrsim E_1$ the structure should become a well-defined peak. With increasing frequency the 2TO(Γ) Raman peak should shift to lower frequencies in germanium because the optical phonon frequency decreases with increasing momentum. All these predictions are in qualitative agreement with the results of Fig. 12. Quantitatively, Fig. 12 suggests a maximum shift of the 2TO(Γ) peak of about 7 cm^{-1}. Figure 14 predicts a change in the important momenta of $X = aQ \approx 10$–15 corresponding to phonon shifts in germanium[25] of about 3–10 cm^{-1} for TO or LO phonons in rough agreement with the experimental value. The line shapes, linewidths, and line shifts behave in many respects similar to the previously considered case of 2LO(Γ), 2TO(Γ) and LO(Γ) + TO(Γ) scattering at the E_0 gap in GaP,[13,26] although in this case a Fröhlich mechanism determines the electron–LO-phonon interaction.

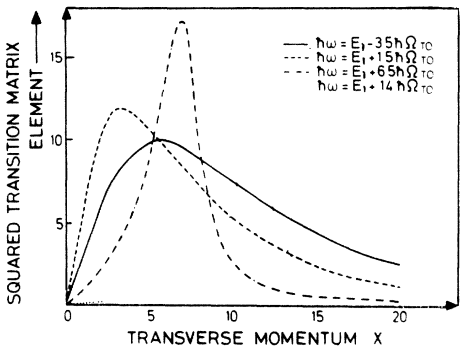

FIG. 14. Squared transition matrix element for the contribution of one [111] valley to the 2TO(Γ) iterative scattering as function of the transverse momentum X: aQ calculated for three incident photon frequencies: solid line: $\hbar\omega = E_1 - 3.5\hbar\Omega_{TO}$; dashed line: $\hbar\omega = E_1 + 1.5\hbar\Omega_{TO}$; dash-dot line: $\hbar\omega = E_1 + 6.5\hbar\Omega_{TO}$; dot line: $\hbar\omega = E_1 + 14\ \hbar\Omega_{TO}$.

Figure 12 also shows a deformation of the relative intensities of the 2TO(L) and the 2TO($X - W$) peaks from 2.41 to 2.6 eV. Figures 7 and 11 suggest that the 2TO(L) structure resonates in excess

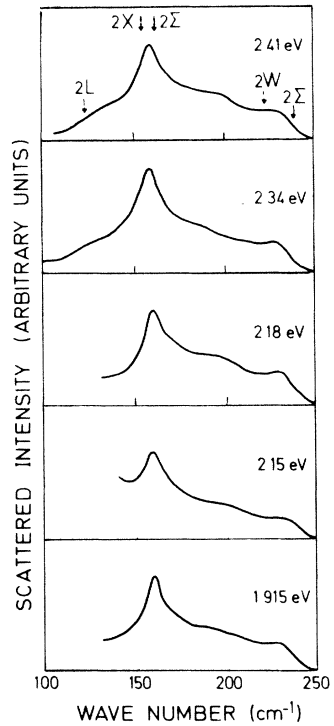

FIG. 15. 2TA Raman spectra of germanium for five different laser frequencies.

of the theoretical electron–two-phonon interaction curve. A possible explanation for this additional cross section is a contribution of iterative processes which for the edge of the zone phonons can become strong near indirect gaps.[19] The phonons which participate in the corresponding indirect absorption show an iterative Raman resonance because of a vanishing energy denominator in the process of Fig. 3(b). The strongest indirect gap, that between the maxima in the density of valence and conduction states, occurs somewhat high in energy[27] (5 eV) to explain the observed iterative L phonon resonance. It is more satisfactory to invoke transitions between the $L_{3'}$ critical point of the valence band and the first maximum in the density of conduction-band states related to the $X-\Sigma$ regions (3.5 eV).[27] The X point is at the low-energy side of this peak, giving an $L_{3'}-X$ gap of 2.6 eV which would explain well the observed iterative 2TO(L) resonance: the momentum transfer at this indirect gap is

$$(2\pi/a)(\tfrac{1}{2},\tfrac{1}{2},\tfrac{1}{2})-(2\pi/a)(1,0,0)$$
$$=(2\pi/a)(-\tfrac{1}{2},\tfrac{1}{2},\tfrac{1}{2})\equiv L \text{ point.}$$

We should point out that an analogous 2Γ resonance has been recently observed for silicon at and above 3.4 eV.[28]

The 2TA Raman spectra are shown in Fig. 15 for five different laser frequencies. Within experimental uncertainties no deformation of the scattering curve with laser frequency occurs.

APPENDIX

We give in the following explicit expressions for the electron-photon and electron-phonon coupling functions appropriate for the E_1 and $E_1+\Delta_1$ gaps in germanium. The coupling functions are defined in such a way that they contain all factors and matrix elements in front of the creation and destruction operators in the Hamiltonian. The symmetry properties of the electron-photon interaction are determined by the momentum operator, those of the electron-phonon interaction by a potential derivative. In the first case one needs the matrix elements between valence and conduction bands, in the second case within the valence and conduction bands. Using the symmetry group C_{3v} and the valence band symmetries $\Lambda_{4,5}$ and Λ_6 and the conduction band symmetry Λ_6 one obtains the coupling matrix

$$\begin{aligned} &g_{1i}=g_{2i}^{*}, \qquad i=x,y,z \\ &g_{1x}=-g_{1y}^{*}=\frac{g}{\sqrt{2}}\left(1\pm\frac{1}{\sqrt{3}}\right), \\ &g_{1z}=\frac{g}{\sqrt{2}}\left(\pm\sqrt{\frac{2i}{3}}\right) \end{aligned} \tag{A1}$$

for the electron-photon matrix. The index i refers to the three Cartesian components of the momentum operator and the indices 1 and 2 to the E_1 and $E_1+\Delta_1$ gaps. The $\pm$ signs correspond to the fact that each band consists of a doublet. g is given by

$$g=-\frac{e}{cm}\left(\frac{2\pi c^2 h}{\omega}\right)^{1/2}\langle c|p_x|v\rangle\,, \tag{A2}$$

where c in the matrix element is the conduction band at the E_1 critical point and v the heavy hole band without spin-orbit splitting which transform as

$$\frac{1}{\sqrt{2}}(X-Y)\,.$$

For the deformation potentials we use the definitions of Kane.[10] We assume that they are independent of the transformed momentum but still can depend on the wave vector of the electron and holes involved in the scattering process.

There is only one constant at the Γ point defined by

$$d_5=(2/3)^{1/2}\langle\Gamma_{25'X}|h_{\Gamma_{25'}z}|\Gamma_{25'Y}\rangle\,. \tag{A3}$$

$|\Gamma_{25'X}\rangle$ is the X component of the three-fold degenerate valence bands at Γ of symmetry $\Gamma_{25'}$. The perturbation $h_{\Gamma_{25'}z}$ is due to optical phonons at Γ and represents a relative displacement of the two sublattices:

$$h_{\Gamma_{25'}z}=2a\frac{\partial V}{\partial u_z}\,. \tag{A4}$$

The vector $\vec{u}$ describes the relative position of

the sublattices and a is the cubic lattice constant. The deformation potential d_0 of Ref. 8 is connected with d_5 by $d_0 = d_5/\sqrt{2}$.

Along the [111] direction there are three independent deformation potential constants, one for the conduction band and two for the valence bands. Neglecting the spin-orbit interaction they are defined by[10]

$$d^5_{1,0}(\text{cond}) = \langle \Lambda_1 | h_{\Lambda_1} | \Lambda_1 \rangle ,$$
$$d^5_{1,0}(\text{val}) = \langle \Lambda_{3,1} | h_{\Lambda_1} | \Lambda_{3,1} \rangle , \tag{A5}$$
$$d^5_{3,0} = \langle \Lambda_{3,1} | h_{\Lambda_{3,2}} | \Lambda_{3,1} \rangle .$$

Here Λ_1 is the conduction band, $\Lambda_{3,1}$ the valence band which transforms as $(1/\sqrt{2}(X-Y)$ and

$$h_{\Lambda_1} = (1/\sqrt{3})(h_{\Gamma^+_{25}X} + h_{\Gamma^+_{25}Y} + h_{\Gamma^+_{25}Z}) , \tag{A6}$$

$$h_{\Lambda_{3,2}} = (1/\sqrt{6})(h_{\Gamma^+_{25}X} + h_{\Gamma^+_{25}Y} - 2h_{\Gamma^+_{25}Z}) . \tag{A7}$$

If the Γ point is approached from the [111] direction the above deformation potentials behave as

$$d^5_{1,0}(\text{cond}) \to 0, \quad d^5_{1,0}(\text{val}) \to -d_0; \quad d^5_{3,0} \to \sqrt{2}\, d_0 . \tag{A8}$$

Using the relation

$$u_\alpha = \left(\frac{\hbar a^3}{4V\Omega M}\right)^{1/2} (a^\dagger_\alpha + a_\alpha) \tag{A9}$$

(M is the mass of the nucleus, $a^\dagger_\alpha$ the creation operator for a TO phonon at Γ of polarization α and Ω the corresponding phonon frequency) and assuming that the deformation potentials are not influenced by the spin-orbit splitting the coupling functions f can easily be worked out along the [111] direction. We obtain for conduction-band scattering

$$f(X) = f(Y) = f(Z) = \frac{1}{4}\left(\frac{6a\hbar}{V\Omega M}\right)^{1/2} d^5_{1,0}(\text{cond}) . \tag{A10}$$

X, Y, Z denote the polarization of the phonon. The scattering in the valence bands is determined by

$$f_{ij}(X) = f^*_{ij}(Y) = \frac{1}{4}\left(\frac{3a\hbar}{V\Omega M}\right)^{1/2} \begin{pmatrix} \sqrt{2}\, d^5_{1,0}(\text{val}) & (1 \mp i\sqrt{3})d^5_{3,0} \\ (1 \pm i\sqrt{3})d^5_{3,0} & \sqrt{2}\, d^5_{1,0}(\text{val}) \end{pmatrix},$$

$$f_{ij}(Z) = \frac{1}{4}\left(\frac{6a\hbar}{V\Omega M}\right)^{1/2} \times \begin{pmatrix} d^5_{1,0}(\text{val}) & -\sqrt{2}\, d^5_{3,0} \\ -\sqrt{2}\, d^5_{3,0} & d^5_{1,0}(\text{val}) \end{pmatrix} . \tag{A11}$$

The indices i, j denote the two spin-orbit split valence bands. The transition amplitude for first-order scattering is

$$T_{\gamma\gamma'}(j) = \sum_{\substack{v,v' \\ \vec{p}}} \frac{g^*_v(\gamma)[f(j)\delta_{vv'} - f_{vv'}(j)]g_{v'}(\gamma')}{[\hbar\omega + i\eta - \hbar\omega_c(\vec{p}) + \hbar\omega_v(\vec{p})][\hbar\omega + i\eta - \hbar\omega_c(\vec{p}) + \hbar\omega_{v'}(\vec{p}) - \hbar\Omega]} . \tag{A12}$$

Using a critical point analysis and the abbreviations (μ is the reduced transverse mass)

$$\alpha_1 = \frac{\hbar\omega + i\eta - \epsilon_1}{\epsilon} , \quad \alpha_2 = \frac{\hbar\omega + i\eta - \epsilon_2}{\epsilon} , \quad \epsilon = \frac{\hbar^2}{2\mu a^2} , \tag{A13}$$

(A12) gives for the Γ'_{25} component of the cross section for first order scattering

$$\frac{d\sigma^{\Gamma'_{25}}}{d\Omega} = \frac{3\omega'^2 VC^2 |g|^4}{4\pi^4 a^5 c^4 \epsilon^4 M\hbar\Omega} \left| \left(\frac{2}{3}\right)^{1/2} d^5_{3,0} \sum_{v \neq v'} \left(\frac{\ln(\alpha_v) - \ln(\alpha_{v'} - \hbar\Omega/\epsilon)}{\alpha_v - \alpha_{v'} + \hbar\Omega/\epsilon} \right. \right.$$
$$\left. \left. + \frac{1}{2\sqrt{3}}[d^5_{1,0}(\text{cond}) - d^5_{1,0}(\text{val})] \sum_{v=1}^{2} \left(\frac{\ln(\alpha_v) - \ln(\alpha_v - \hbar\Omega/\epsilon)}{\hbar\Omega/\epsilon} \right) \right|^2 . \tag{A14}$$

C is a cutoff for the longitudinal $\vec{p}$ sum and about $\frac{2}{3}$ for Ge. The content of the bracket is proportional to d_1 of Eq. (3) and agrees with Eq. (3) because $\chi^+ \sim \ln(\alpha_1)$, $\chi^- \sim \ln(\alpha_2)$, $\chi = \chi^+ + \chi^-$.

*On leave from the Laboratoire de Physique Expérimental, Université Paul Sabatier, Toulouse, France.

[1]See articles in *Light Scattering in Solids*, edited by M. Balkanski (Flammarion, Paris, 1971).
[2]See articles in *Light Scattering Spectra of Solids*, edited by G. B. Wright (Springer-Verlag, New York, 1969).
[3]M. Cardona, Surf. Sci. 37, 100 (1973).
[4]F. Cerdeira, W. Dreybrodt, and M. Cardona, Solid State Commun. 10, 591 (1972).
[5]P. Y. Yu and Y. R. Shen, Phys. Rev. Lett. 29, 468 (1972).
[6]M. I. Bell, R. N. Tyte, and M. Cardona, Solid State Commun. 13, 1833 (1973).
[7]B. A. Weinstein and M. Cardona, Phys. Rev. B 8, 2795 (1973).
[8]M. Cardona, *Atomic Structure and Properties of Solids*, edited by E. Burstein (Academic, New York, 1972), p. 514.
[9]O. G. Peterson, S. A. Tuccio, and B. B. Snavely, Appl. Phys. Lett. 17, 245 (1970).
[10]E. O. Kane, Phys. Rev. 178, 1368 (1969).
[11]M. A. Renucci, J. B. Renucci, and M. Cardona, Solid State Commun. 14, 1299 (1974).
[12]M. A. Renucci, J. B. Renucci, and M. Cardona, Ref. 1, p. 326.
[13]B. A. Weinstein and M. Cardona, Phys. Rev. B 7, 2545 (1973).
[14]R. Loudon, Adv. in Physics 13, 423 (1964).

[15]D. D. Sell and E. O. Kane, Phys. Rev. 185, 1103 (1969).
[16]F. H. Pollak and M. Cardona, Phys. Rev. 172, 816 (1968).
[17]R. F. Potter, Phys. Rev. 150, 562 (1966).
[18]M. Cardona and F. H. Pollak, Phys. Rev. 142, 530 (1966).
[19]P. B. Klein, H. Masui, Jin-Joo Song and R. K. Chang, Solid State Commun. (to be published).
[20]P. Y. Yu and Y. R. Shen, Phys. Rev. Lett. 32, 939 (1970).
[21]K. Ganguly and J. L. Birman, Phys. Rev. 162, 806 (1967).
[22]W. Dreybrodt, W. Richter, and M. Cardona, Solid State Commun. 11, 1127 (1972).
[23]I. Goroff and L. Kleinman, Phys. Rev. 132, 1080 (1963).
[24]M. Cardona, *Modulation Spectroscopy* (Academic, New York, 1969).
[25]G. Nelin and G. Nilssen, Phys. Rev. B 5, 3151 (1972).
[26]R. Zeyher, Phys. Rev. B 9, 4439 (1974).
[27]F. Herman, R. L. Kortum, C. C. Kuglin and J. L. Shay, *II-VI Semiconducting Compounds*, edited by D. G. Thomas (Benjamin, New York, 1967), p. 503.
[28]R. Tyte, J. B. Renucci, and M. Cardona (unpublished).